Monthly Notices of the ROYAL ASTRONOMICAL SOCIETY

MNRAS **516,** 2062–2073 (2022) https://doi.org/10.1093/mnras/stac1767
Advance Access publication 2022 June 25

Searching for the connection between ionizing-photon escape and the surface density of star formation at $z \sim 3$

Anthony J. Pahl [1]★ Alice Shapley,[1] Charles C. Steidel,[2] Naveen A. Reddy[3] and Yuguang Chen [2,4]

[1]*Department of Physics and Astronomy, University of California, Los Angeles, CA 90095, USA*
[2]*Cahill Center for Astronomy and Astrophysics, California Institute of Technology, MC249-17, Pasadena, CA 91125, USA*
[3]*Department of Physics and Astronomy, University of California Riverside, Riverside, CA 92521, USA*
[4]*Department of Physics and Astronomy, University of California Davis, 1 Shields Avenue, Davis, CA 95616, USA*

Accepted 2022 June 21. Received 2022 April 29; in original form 2022 January 31

ABSTRACT

The connection between the escape fraction of ionizing photons ($f_{\rm esc}$) and star formation rate surface density ($\Sigma_{\rm SFR}$) is a key input for reionization models, but remains untested at high redshift. We analyse 35 $z \sim 3$ galaxies from the Keck Lyman Continuum Survey (KLCS) covered by deep, rest far-UV spectra of the Lyman continuum (LyC) and high-resolution *HST* V_{606} imaging, enabling estimates of both $f_{\rm esc}$ and rest-UV sizes. Using Sérsic profile fits to *HST* images and spectral-energy distribution fits to multiband photometry, we measure effective sizes and SFRs for the galaxies in our sample, and separate the sample into two bins of $\Sigma_{\rm SFR}$. Based on composite spectra, we estimate $\langle f_{\rm esc} \rangle$ for both $\Sigma_{\rm SFR}$ subsamples, finding no significant difference in $\langle f_{\rm esc} \rangle$ between the two. To test the representativeness of the KLCS *HST* sample and robustness of this result, we attempt to recover the well-established correlation between $f_{\rm esc}$ and Lyα equivalent width. This correlation is not significant within the KLCS *HST* sample, indicating that the sample is insufficient for correlating $f_{\rm esc}$ and galaxy properties such as $\Sigma_{\rm SFR}$. We perform stacking simulations using the KLCS parent sample to determine the optimal sample size for robust probes of the $f_{\rm esc}$-$\Sigma_{\rm SFR}$ connection to inform future observing programs. For a program with a selection independent of ionizing properties, $\geq$90 objects are required; for one preferentially observing strongly-leaking LyC sources, $\geq$58 objects are required. More generally, measuring the connection between $f_{\rm esc}$ and $\Sigma_{\rm SFR}$ requires a larger, representative sample spanning a wide dynamic range in galaxies properties such as $\Sigma_{\rm SFR}$.

Key words: galaxies: high-redshift – cosmology: observations – dark ages, reionization, first stars.

1 INTRODUCTION

Reionization is a key phase transition of the Universe in which the neutral hydrogen in the intergalactic medium (IGM) becomes ionized. While the reionization process concludes by $z \sim 6$ (Fan, Carilli & Keating 2006), the overall evolution of the hydrogen neutral fraction depends on our understanding of the population of the first star-forming galaxies that are thought to emit the bulk of the ionizing photons into the IGM (e.g. Parsa, Dunlop & McLure 2018). The ionizing emissivity as a function of cosmic time can be simply parametrized as the product of the comoving UV luminosity density ($\rho_{\rm UV}$), ionizing photon efficiency ($\xi_{\rm ion}$), and escape fraction of ionizing photons that go on to ionize the surrounding H I gas ($f_{\rm esc}$) (Robertson et al. 2015). These parameters and their redshift dependence must be characterized beyond $z \sim 6$ to construct a complete picture of reionization.

The most difficult of the three parameters to constrain is $f_{\rm esc}$, for which estimates rely on direct measurement of the Lyman continuum (LyC; $\lambda < 912$Å) spectral region. Due to the large cross-section of H I to LyC photons, even a small neutral fraction (< 1 per cent) can attenuate this signal, thus direct observations become prohibitive at $z \gtrsim 4$ (Vanzella et al. 2012; Steidel et al. 2018). We must use lower-redshift galaxies to obtain direct measurements of escaping LyC emission at the highest redshift where the measurements are possible, and, simultaneously, connect their properties with those of ionizing sources at $z > 6$. To this end, large-scale LyC surveys have attempted to measure the average $f_{\rm esc}$ of galaxies at $z \sim 2$–4 and to understand the mechanisms of LyC escape. These surveys either attempt to detect LyC photometrically (Grazian et al. 2017; Fletcher et al. 2019; Nakajima et al. 2019; Saxena et al. 2021) or spectroscopically (Marchi et al. 2017, 2018). Of particular note is the Keck Lyman Continuum Spectroscopic Survey (KLCS), which includes 124 objects selected as Lyman Break Galaxies (LBGs) with $\langle f_{\rm esc} \rangle = 0.09 \pm 0.01$ measured through deep, rest-UV spectroscopy (Steidel et al. 2018). A subset of 39 KLCS galaxies was followed up with *Hubble Space Telescope* (*HST*) multiband imaging, including all galaxies with apparent individual LyC detections. These observations were designed to eliminate the effects of foreground contamination on the average measurements, a significant concern for detecting LyC leakers at $z \sim 3$ (Vanzella et al. 2012; Mostardi et al. 2015). In Pahl et al. (2021), we reported that four KLCS galaxies (two of which had been identified as significant leakers) imaged by *HST* had multiband photometry consistent with low-redshift interlopers, and updated the average $f_{\rm esc}$ of the KLCS sample to 0.06 ± 0.01 after removing these four galaxies.

Within these studies, one of the parameters that positively correlates with LyC leakage is the equivalent width of Lyα emission

★ E-mail: pahl@astro.ucla.edu

(W_λ(Lyα)), in the sense that galaxies with higher W_λ(Lyα) have higher f_{esc} on average (Marchi et al. 2017, 2018; Steidel et al. 2018; Pahl et al. 2021). This correlation suggests that Lyα and LyC leakage in star-forming galaxies are connected because of their similar escape pathways through the interstellar and circumgalactic media (ISM and CGM). Since Lyα emission has been found to be inversely correlated with the neutral gas covering fraction both in the local Universe and at $z \sim 3$ (Reddy et al. 2016b; Gazagnes et al. 2020), it follows that a 'picket fence' arrangement of H I would simultaneously modulate LyC emission along with Lyα. The galaxy properties that favour this configuration are an active area of study, and further characterization of the dependence of f_{esc} on galaxy properties is necessary to disentangle this physical picture.

Recently, Naidu et al. (2020) proposed a model of reioniziation in which a galaxy's f_{esc} is solely a function of its star formation rate (SFR) surface density (Σ_{SFR}). This model implies that the bulk of ionizing photon leakage at $z > 6$ can be attributed to relatively luminous and massive galaxies ($M_{UV} < -18$ and $\log(M_*/M_\odot) > 8$), in stark contrast to models that favour the dominant role of dwarf galaxies at $M_{UV} > -15$ (e.g. Finkelstein et al. 2019). The parametrization of f_{esc} as a function of Σ_{SFR} is motivated by the above-average Σ_{SFR} found in many individual LyC detections at $z \sim 2-4$ (De Barros et al. 2016; Shapley et al. 2016; Vanzella et al. 2016; Bian et al. 2017; Vanzella et al. 2018), as well as in the *HST*/COS sample of LyC detections at $z \sim 0.3$ (Borthakur et al. 2014; Izotov et al. 2016, 2018, 2021). Additionally, the survey of Marchi et al. (2018) found that stacks of galaxies with small UV spatial size had a significantly higher average LyC flux than those with larger size, implying that compact galaxies have conditions favourable for LyC escape. The spectroscopic survey of Reddy et al. (2022) found Lyα escape can be aided by a high Σ_{SFR}, especially in low stellar mass galaxies. Finally, hydrodynamic simulations, including radiative transfer, such as those of Ma et al. (2016), predict that feedback from massive stars carves channels in the ISM that allow for efficient leakage of LyC. This effect is predicted to be most pronounced in galaxies containing a high density of star formation. The f_{esc}-Σ_{SFR} paradigm has important implications for testing the model of reionization presented by Naidu et al. (2020), and for informing the evolution of the H I fraction, but has not been confirmed observationally in a large-scale survey with selection criteria independent of Σ_{SFR}.

In this work, we attempt the first LBG-selected study of f_{esc} as a function of Σ_{SFR} using the subset of KLCS galaxies covered by *HST* imaging. Thanks to the high-resolution *HST* imaging offered by Pahl et al. (2021), well-constrained size measurements are possible for the first time for 35 of the galaxies in KLCS, including the 13 with significant individual LyC detections. Combined with the ability to estimate SFRs from the wealth of multiband photometry available for KLCS, this subsample is ideal for the first observational test of of the connection between ionizing photon escape and Σ_{SFR}. Using the deep, rest-frame UV spectra of KLCS, which include coverage of LyC at rest-frame 880−910 Å; at $z \sim 3$, these spectra can be stacked as a function of Σ_{SFR} to explore characteristics of the LyC spectral region. While stacking reduces the uncertainty due to line-of-sight variations in IGM transmission, it remains to investigate whether this KLCS *HST* subsample is adequate to constrain any dependence of f_{esc} on Σ_{SFR}.

The structure of the paper is as follows: in Section 2, we describe the observations and data available for the KLCS *HST* sample. In Section 3, we describe the SFR and size measurements, which we present in Section 4 alongside descriptions and measurements of the composite spectra constructed in two bins of Σ_{SFR}. In Section 5, we examine the robustness of the KLCS *HST* sample for quantifying the correlation between f_{esc} and Σ_{SFR}, and perform simulations to determine the minimum sample composition for analyzing the relationship between the escape of ionizing radiation and galaxy properties. We summarize our conclusions in Section 6.

Throughout this paper, we adopt a standard ΛCDM cosmology with $\Omega_m = 0.3$, $\Omega_\Lambda = 0.7$, and $H_0 = 70$ km s^{-1}Mpc^{-1}. The f_{esc} values reported in this paper are absolute escape fractions, equivalent to $f_{esc,\,abs}$ in Steidel et al. (2018), and defined as the fraction of all H-ionizing photons produced within a galaxy that escapes into the IGM. We also employ the AB magnitude system (Oke & Gunn 1983).

2 SAMPLE

The KLCS (Steidel et al. 2018) includes an analysis of the hydrogen-ionizing spectra of 137 galaxies selected as LBGs (for details of selection see Steidel et al. 2003; Adelberger et al. 2004; Reddy et al. 2012). To this end, deep optical spectra were obtained using the Low-Resolution Imaging Spectrometer (LRIS; Oke et al. 1995; Steidel et al. 2004) on the Keck I telescope, covering the LyC spectral region, as well as the Lyα feature and far-UV metal absorption lines. These data were taken with total exposure times per mask of ∼10 hrs. Thirteen galaxies were removed from the sample due to clear evidence of blending, the presence of instrumental defects, or with evidence of multiple spectroscopic redshifts, for a final analysis sample of 124 objects. Steidel et al. (2018) characterized the escaping ionizing signal from each galaxy using the average flux density in the wavelength region 880Å; − 910Å;, or f_{900}. Fifteen galaxies with significant LyC escape (defined as $f_{900} > 3\sigma_{900}$, where σ_{900} is the error on the flux density in the LyC wavelength region) were defined as the LyC detection sample. The remaining 109 galaxies were characterized as individual LyC non-detections. Despite the best efforts to clean the sample of interloper contamination, high-resolution imaging is necessary for identifying all low-redshift interlopers along the line of sight that frequently contaminate apparent LyC flux for $z \sim 3$ galaxies (Vanzella et al. 2012; Mostardi et al. 2015).

In Pahl et al. (2021), the 15 LyC detection candidates from KLCS were followed up as part of a Cycle 25 *HST* Program ID 15287 (PI: Shapley) in order to explore the effects of foreground contamination in the KLCS sample. While these LyC detection candidates were specifically targeted as the most likely sources of contamination due to their significant individual f_{900} measurements, 24 LyC individual non-detections were also observed as they fell within the field of view of the *HST* pointings. These 39 objects were observed with ACS/F606W (V_{606}), WFC3/F125W (J_{125}), and WFC3/F160W (H_{160}) between 2017 and 2019 in five KLCS survey fields (Q0933, Q1422, DSF2237b, Q1549, and Westphal). Additional *HST* data were included from Mostardi et al. (2015) and Shapley et al. (2016) for one object, Q1549-C25. The seven ACS pointings and 11 WFC3 pointings were observed for three orbits per filter. We used $V_{606}J_{125}H_{160}$ photometry to characterize the contamination likelihood of individual subcomponents within the LyC detection sample, following the methodology of Mostardi et al. (2015). To this end, two LyC detections were determined to be likely contaminated and were subsequently removed from the sample. Similar contamination analysis was performed on the objects with individual LyC non-detections for completeness. Two galaxies with individual non-detections had subcomponents with $V_{606}J_{125}H_{160}$ photometry consistent with low-redshift interlopers, thus these objects were also removed, for a remaining KLCS *HST* sample of 35.

We use this 'KLCS *HST*' sample of 35 objects that were determined to be free of contamination for the analysis presented here. While all KLCS objects have multiband photometry that can be used to estimate the SFR through spectral-energy distribution (SED) fitting, only those targeted by *HST* have the higher resolution imaging necessary to measure accurate rest-UV sizes. In this KLCS *HST* sample, there are 13 galaxies with individual LyC detections, and 22 galaxies with individual LyC non-detections, as defined by Steidel et al. (2018). Thus, the KLCS *HST* subsample is biased in favour of LyC detections compared to the full sample, which contains 13 individual LyC detections out of a total of 120 galaxies. We discuss the effects of this selection bias in Section 4.

3 METHODOLOGY

In this section, we present the steps necessary to measure $\Sigma_{\rm SFR}$ for the KLCS *HST* sample. This measurement requires sizes, estimated by fitting the 2D light profiles in *HST* imaging, and SFRs, calculated from SED fitting.

3.1 Sizes

We estimated the sizes of objects in our sample from model fits to the light distributions in the V_{606} images, which have the highest resolution within our *HST* data set. For this modelling, we used the software GALFIT (Peng et al. 2002, 2010), which uses parametric fits of one or more Sérsic profiles and a uniform sky background to the 2D postage stamp of a galaxy. At the redshifts of our sample galaxies, single Sérsic profiles have been demonstrated to reasonably constrain the effective sizes of distinct morphological components in *HST* imaging (Law et al. 2012; Van Der Wel et al. 2012; Shibuya, Ouchi & Harikane 2015; Gillman et al. 2020). We follow Van Der Wel et al. (2012), who presented robust measurements using Sérsic profiles of basic morphological properties such as half-light radii for galaxies in the CANDELS survey down to $H_{160} \sim 24.5$.

The free parameters of the fits are central position (x, y), magnitude, Sérsic index (n), position angle, axial ratio (b/a), and half-light radius along the major axis (r) for each profile, as well as a uniform sky background level. One of the inputs to the GALFIT modelling is a bad-pixel mask for each object based on the segmentation map produced by SEXTRACTOR (Bertin & Arnouts 1996). The SEXTRACTOR detection threshold was set at 2.5 times the background RMS, and the background was estimated using the 'local' setting, which estimates the sky contribution using a rectangular annulus. All components unrelated to the central object were masked, ensuring that the flux from surrounding sources does not affect the fit. Deconvolution was performed using point-spread functions (PSFs) described in Pahl et al. (2021). These PSFs were constructed for each field by averaging 10−15 unsaturated stars in the V_{606} mosaic using the ASTROPY routine *Photutils* (Bradley et al. 2020).

We initialized the positions of the Sérsic profiles for each object using the central coordinates of up to three of the brightest components deblended with SEXTRACTOR. We set an initial guess of $n = 4$ and $r = 5$ pixels. The initial guesses for the magnitude of each source and the sky background level were drawn from the SEXTRACTOR catalogs. After fitting, the residuals were inspected by eye to ensure that the background levels were properly subtracted and the models accurately described the radial extent of the light profile. In the top three panels of Fig. 1, the fitting process is detailed for the galaxy Q1549-D3, with the *HST* V_{606} image, model fit, and residual displayed from left to right.

To estimate an effective size for objects with single-component fits, we calculated the circularized effective radius ($r_{\rm e}$) by combining the best-fitting r and b/a parameters from GALFIT according to $r_{\rm e} = r\sqrt{b/a}$. We defined the effective area of the galaxy as $\pi r_{\rm e}^2$, which corresponds to the projected area containing half of the total light of the galaxy.

For objects with multicomponent fits, we estimated the effective area using the best-fitting model produced by GALFIT. By using the best-fitting model without the PSF convolution, we effectively recreated the deconvolved image for each object. We integrated this deconvolved model to find a total flux F, then sorted the pixels in brightness. A number $n_{\rm pix}$ of the brightest pixels were chosen, starting at the brightest pixel and continuing towards fainter pixels, such that the integrated flux contained within $n_{\rm pix}$ was $F/2$. The effective area of an object was then found by applying the *HST* V_{606} pixel scale of $0.03''$/pix, which we subsequently converted to a circularized radius using $n_{\rm pix} \times (0.03(''/{\rm pix}))^2 = \pi r_{\rm e}^2$.

We pursued an empirical approach for estimating the errors on the effective sizes of the galaxies in our sample. We randomly perturbed each pixel of the science image by a value drawn from a Gaussian distribution with standard deviation corresponding to the pixel value in the error image generated from the reduction process of the *HST* V_{606} imaging (See Section 3.2; Pahl et al. 2021). To ensure our error bars encapsulated any systematic error induced by different initial guesses, we also randomly perturbed the initial guesses of all model parameters. Starting with the best-fitting parameters from the unperturbed fit, we perturbed the x and y positions by a Gaussian distribution with width 2 pixels, and multiplied r by a factor drawn from a Gaussian distribution with a mean of 1.0 and a standard deviation of 0.3. We randomized n uniformly between 0.5 and 4.0, and a/b between 0.0 and 1.0. We then fit the perturbed science image with these randomized initial guesses following the methods described above and subsequently measured $r_{\rm e}$. After 100 realizations, the standard deviation of the $r_{\rm e}$ distribution was taken as the error on the object's $r_{\rm e}$ measurement. These empirically determined errors are comparable to those calculated internally by GALFIT for the objects with single-Sérsic fits.

We present the postage stamps and sizes of the 35 KLCS *HST* objects in Fig. 1. Displayed in cyan are curves containing the effective areas: for single-component morphologies, these are defined by the Sérsic model parameters r and a/b, and, for multicomponent morphologies, the cyan curves enclose the pixels corresponding to the half-light area as described above. In the bottom-right corner of each panel, we present the circularized $r_{\rm e}$ for each object in both angular (arcsec) and physical (kpc) size. Displayed in black is the LRIS slit for each object: all components that contribute to the $r_{\rm e}$ measurement are contained within the slit for KLCS *HST* targets.

3.2 Star formation rates

We fit multiband photometry available for our objects with stellar population synthesis models in order to derive galaxy properties such as stellar mass (M_*), $E(B-V)$, stellar age, and SFR. While the SFR measurement is the focus of this work, we will explore other derived galaxy properties of KLCS in future work.

We measured $V_{606}J_{125}H_{160}$ photometry for the KLCS *HST* objects based on *HST* images reduced and described in Pahl et al. (2021). We followed a similar measurement procedure to that of Pahl et al. (2021), however, for consistency with the ground-based measurements, we set the detection threshold used with SEXTRACTOR to 2.5 times the background RMS, and removed any deblending to get singular measurements for each object.

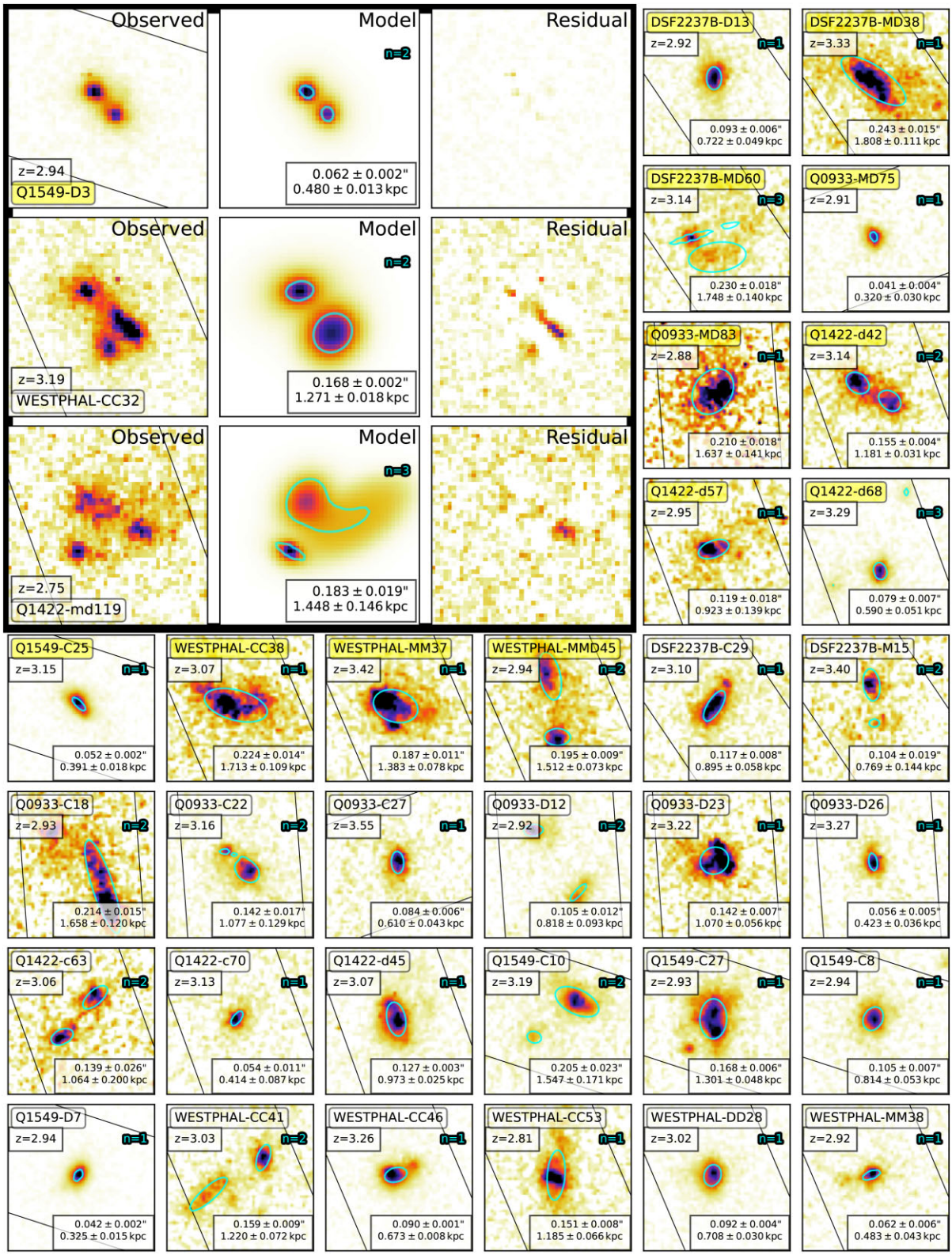

Figure 1. V_{606} postage stamps of the 35 galaxies in KLCS *HST*. The panels in the upper left show the *HST* V_{606} image, the GALFIT model, and the residual, from left to right, for three objects to demonstrate the fitting process. The cyan curve shows the effective area of each object and the black lines show the LRIS slit (1.2 arcsec wide) for each object. Displayed in the bottom right of each panel is the circularized r_e in both angular size (arcsec) and physical (kpc) size. Displayed in the middle right of each panel in cyan are the number of Sérsic profiles used in the model fit. Objects with individual LyC detections have object names highlighted in yellow. All panels are 1.5 arcsec per side.

Table 1. Photometric bands used in SED modelling.

Fields	Photometric bands
DSF2237b	U_n^a, G^a, R_s^a, I^a, J^b, K_s^b, IRAC1, IRAC2, V_{606}, J_{125}, H_{160}
Q0933	U_n^a, G^a, R_s^a, I^a, J^b, K_s^b, IRAC1, IRAC2, V_{606}, J_{125}, H_{160}
Q1422	U_n^c, G^c, R_s^c, K_s^b, IRAC1, IRAC2, V_{606}, J_{125}, H_{160}
Q1549	U_n^d, G^d, R_s^d, J^f, H^f, $K_s^{b,f}$, IRAC1, IRAC2, IRAC3, V_{606}, J_{125}, H_{160}
Westphal	u∗^{g}, g'^{g}, r'^{g}, i'^{g}, z'^{g}, J^h, H^h, K_s^h, IRAC1, IRAC2, V_{606}, J_{125}, H_{160}

[a]Observed with the COSMIC prime focus imager on the Palomar 5.08 m telescope (see Steidel et al. 2003).
[b]Observed with the Multi-Object Spectrograph for Infra-Red Exploration (MOSFIRE) on the Keck I telescope.
[c]Observed with the Prime Focus Imager on the William Herschel 4.2m telescope (see Steidel et al. 2003).
[d]Observed with Keck/LRIS.
[f]Observed with FourStar at the Magellan Baade 6.5 m telescope.
[g]From the Canada-France-Hawaii Telescope (CFHT) Legacy Survey.
[h]Observed with CFHT/WIRCam as part of the WIRCam Deep Survey (Bielby et al. 2012).

For additional input photometry that constitute the KLCS *HST* SEDs, we used a multitude of data available for the objects in the survey fields (e.g. Reddy et al. 2012). At minimum, all five fields were covered by ground-based U_nGR_s optical, K_s near-IR, and *Spitzer*/IRAC Channels 1 and 2 infrared imaging. Some fields had additional photometric information, as summarized in Table 1. For objects with a clear K_s excess, we performed corrections to the broadband flux based on measured fluxes of the strong emission lines of [O III] and H α (Steidel et al. 2014).

We measured the SFRs for each object using SED fitting based on the methods described in Reddy et al. (2018). Specifically, we used Bruzual & Charlot (2003) stellar population synthesis models and assumed a Salpeter (1955) initial mass function (IMF). We note that, using the stellar population synthesis models of BPASS (BPASS v2.1; Eldridge et al. 2017) and assuming the same IMF, we find excellent agreement for the inferred SFRs. A constant star formation history with stellar ages no younger than 50 Myr was assumed, such that stellar ages would not extend to younger ages than the typical dynamical time-scales of star-forming galaxies at $z \sim 3$ (Reddy et al. 2012). We fit the SEDs using two sets of assumptions for metallicity and dust attenuation curve: 0.28 times solar metallicity and an SMC extinction curve (i.e. $0.28Z_\odot$ + SMC, Gordon et al. 2003), and 1.4 times solar metallicity and a Calzetti et al. (2000) extinction curve (i.e. $1.4Z_\odot$ + Calzetti). For two galaxies with $\log(M_*/M_\odot)>10.65$ measured using the $0.28Z_\odot$ + SMC models, we adopted the $1.4Z_\odot$ + Calzetti model for the final fit, based on systematically better fits to the observed SEDs in Du et al. (2018) and for consistency with the mass–metallicity relation (Steidel et al. 2014; Sanders et al. 2015; Onodera et al. 2016). With the exception of the fits to these two galaxies, we adopted $0.28Z_\odot$ + SMC models.

To ensure robust SED fits, we individually examined the input photometry, best-fitting model, and resulting unreduced χ^2 for each object. Due to the higher S/N of *HST*, we removed MOSFIRE or WIRCAM J, H, and K_s data that were inconsistent with *HST* J_{125}, as long as the IRAC photometry constrained the SED redward of the Balmer break. We also removed IRAC photometry that appeared to be blended with other nearby sources. Additionally, we removed any ground-based photometry if the ground-based extraction may have included contamination from nearby objects identified with the higher-resolution *HST* imaging. After eliminating clearly problematic photometry, we achieved SED fits with unreduced $\chi^2 < 30$ for all 35 objects.

4 RESULTS

In this section, we present the $\Sigma_{\rm SFR}$ measurements for the KLCS *HST* sample and the ionizing and non-ionizing spectral properties of the sample as a function of $\Sigma_{\rm SFR}$.

We present the r_e and SFR measurements for our sample in the left-hand panel of Fig. 2. The median r_e is 0.97 kpc (for a median $M_{\rm UV} = -20.7$), comparable to $1.054^{+1.154}_{-0.436}$ kpc found for $z \sim 3$–4 star-forming galaxies at $M_{\rm UV} = -21.0$ (Shibuya et al. 2015). The median SFR of the sample is 14.0 $M_\odot\,{\rm yr}^{-1}$. For each object, we calculate the $\Sigma_{\rm SFR}$ by assuming half of the star formation occurs within the half-light area, such that

$$\Sigma_{\rm SFR} = {\rm SFR}/(2 \times \pi r_e^2), \quad (1)$$

where SFR is inferred from the best-fitting SED model described in Section 3.2, and r_e is the circularized half-light radius measured for each object in Section 3.1. We present the resulting $\Sigma_{\rm SFR}$ distribution in the right-hand panel of Fig. 2. The median $\Sigma_{\rm SFR}$ is 2.81 $M_\odot\,{\rm yr}^{-1}\,{\rm kpc}^{-2}$, which is within the 16th and 84th percentile of the $\Sigma_{\rm SFR}$ relation from Shibuya et al. (2015) with comparable redshift and $M_{\rm UV}$.

In order to examine the ionizing and non-ionizing spectral properties of the KLCS *HST* sample as a function of $\Sigma_{\rm SFR}$, we split the sample into two bins: $\Sigma_{\rm SFR,\,low}$, which contains the 17 galaxies with the lowest $\Sigma_{\rm SFR}$, and $\Sigma_{\rm SFR,\,high}$, which contains the 18 galaxies with the highest $\Sigma_{\rm SFR}$. The two bins are differentiated by black and orange colour for $\Sigma_{\rm SFR,\,low}$ and $\Sigma_{\rm SFR,\,high}$, respectively, in Fig. 2. The median properties of the samples are summarized in Table 2.

We then created composite spectra as described in Steidel et al. (2018) and Pahl et al. (2021) in order to explore spectral differences between the $\Sigma_{\rm SFR,\,low}$ and $\Sigma_{\rm SFR,\,high}$ samples and constrain the dependence of LyC ionizing photon escape on $\Sigma_{\rm SFR}$. The rest-frame UV, LRIS spectra of Steidel et al. (2018) covering the LyC region are normalized to the average flux density within the spectral region $1475 \leq \lambda_0/\text{Å} \leq 1525$ (f_{1500}). We use a spline interpolation to place the spectra on a common wavelength grid, then use a mean combination at each wavelength increment to create the final composite after applying 3σ outlier rejection.

Building spectral composites smooths out variations in IGM sightlines. However, the aggregate effect of the IGM and circumgalactic medium (CGM) strongly attenuates the LyC region at $z \sim 3$. To account for this attenuation, we correct the composites using IGM + CGM transmission functions calculated in a manner

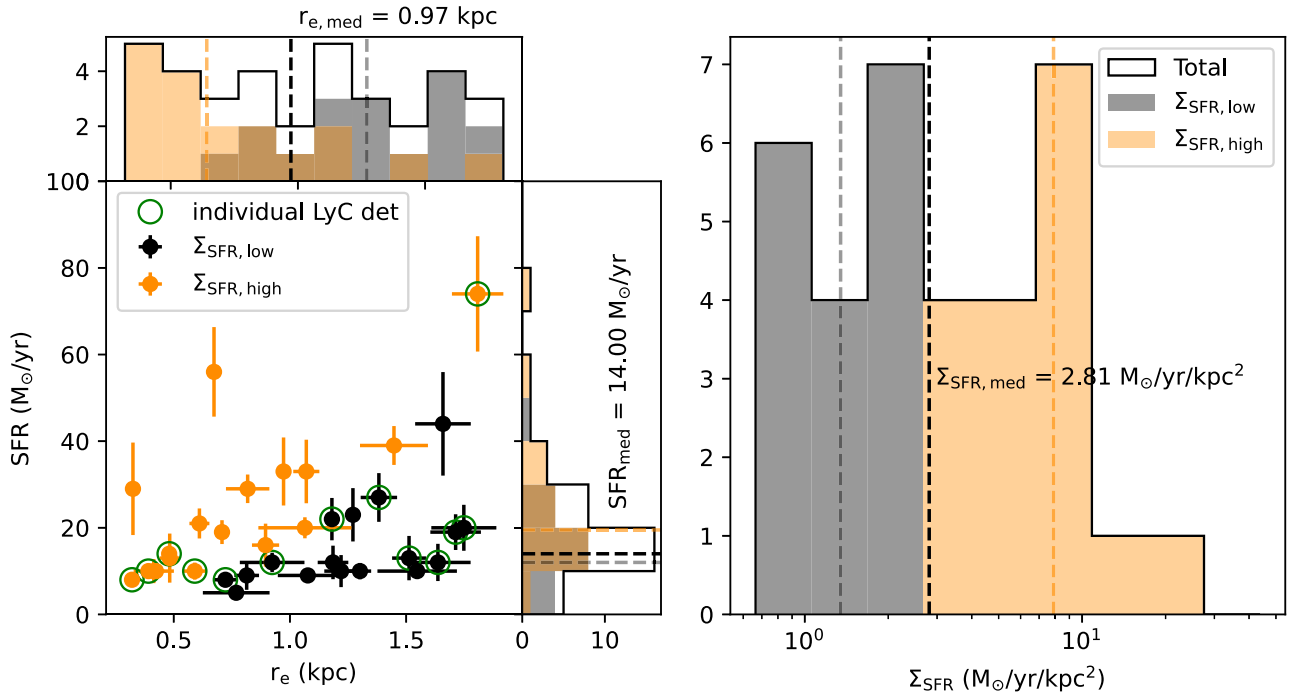

Figure 2. r_e, SFR, and Σ_{SFR} measurements for the KLCS *HST* sample. The 35 objects are split into two bins of Σ_{SFR}: $\Sigma_{SFR,low}$ contains the 17 objects with the lowest Σ_{SFR}, and $\Sigma_{SFR,high}$ contains the 18 objects with the highest Σ_{SFR}. Objects in the $\Sigma_{SFR,low}$ bin are displayed as black points in the scatter plot and black bars in the histograms, while objects in the $\Sigma_{SFR,high}$ bin are displayed as orange points and orange bars. The 13 objects with individual LyC detections are highlighted with a green circle. **Left:** the SFR-r_e distribution of the sample. The dark, black line in the vertical and horizontal histograms show the total r_e and SFR distributions. The sample medians are shown by dashed lines, with the $\Sigma_{SFR,low}$ medians in grey, the $\Sigma_{SFR,high}$ medians in orange, and the total sample median in black. **Right:** the Σ_{SFR} distribution of the sample, calculated according to equation (1). The colour convention follows the histograms in the left-hand panel.

Table 2. Median properties of the two Σ_{SFR} subsamples and resulting composite spectra.

	$r_{e,med}$ (kpc)	SFR_{med} ($M_\odot yr^{-1}$)	$\Sigma_{SFR,med}$ ($M_\odot yr^{-1} kpc^{-2}$)	W_λ(Lyα) (Å)	W_λ(LIS) (Å)	W_λ(HIS) (Å)	$\langle f_{900}/f_{1500}\rangle_{out}$	$f_{esc,abs}$
$\Sigma_{SFR,low}$	1.27 ± 0.11	12.0 ± 2.4	1.35 ± 0.40	10.7 ± 4.9	1.78 ± 0.21	2.81 ± 0.32	0.104 ± 0.013	0.120 ± 0.009
$\Sigma_{SFR,high}$	0.64 ± 0.12	19.5 ± 4.6	7.89 ± 1.53	19.1 ± 10.8	1.66 ± 0.20	3.20 ± 0.32	0.076 ± 0.013	0.122 ± 0.010

consistent with that in Steidel et al. (2018). Notably, for the KLCS *HST* objects, we choose a transmission function drawn from the third quartile of IGM transparency, as opposed to the average transmission used for the composites of Steidel et al. (2018). This decision is based on the oversampling of objects with individual LyC detections in the KLCS *HST* sample (13 detections out of 35 objects) compared to the full KLCS sample (13 detections out of 120 objects, see Section 2). Preferentially targeting individually detected LyC candidates has the approximate effect of choosing IGM sightlines that are more transparent to LyC photons, on average, considering that part of the variation in observed ionizing signal at $z \sim 3$ is due to differences in IGM opacity (Steidel et al. 2018). Assuming the LyC individual detections are drawn from the top 11 per cent of IGM transmission[1] and the 22 LyC non-detections have average sightlines, we consider the third-quartile transmission function as a reasonable approximation of the IGM transmission for the KLCS *HST* sample bins. Below, we discuss the results based on a different assumption for IGM transmission, demonstrating that our key conclusions do not change.

The $\Sigma_{SFR,low}$ and $\Sigma_{SFR,high}$ composite spectra, corrected for IGM + CGM attenuation, are shown in Fig. 3. The LyC region (880 $\leq \lambda_0$/Å; $\leq$ 910) is visually demarcated by dotted-red lines. We calculated the average ionizing flux density of each composite within this region and defined it as $\langle f_{900}\rangle$. The ratio of ionizing to non-ionizing flux density, with f_{900} corrected for effects of the IGM and CGM, is $\langle f_{900}/f_{1500}\rangle_{out} = 0.104 \pm 0.013$ for the $\Sigma_{SFR,low}$ composite and $\langle f_{900}/f_{1500}\rangle_{out} = 0.076 \pm 0.013$ for the $\Sigma_{SFR,high}$ composite. Both of these $\langle f_{900}/f_{1500}\rangle_{out}$ measurements are significantly elevated from the full, uncontaminated KLCS sample measurement of $\langle f_{900}/f_{1500}\rangle_{out} = 0.015 \pm 0.02$ (Pahl et al. 2021). Again, this difference is expected due to the larger proportion of individually detected LyC galaxies in KLCS *HST*. We summarize the sample composition of each Σ_{SFR} bin in Table 3 and the properties of each KLCS *HST* galaxy. In $\Sigma_{SFR,low}$, 8/17 galaxies are LyC individual detections and in $\Sigma_{SFR,high}$, 5/18 galaxies are individually detected.

The property $\langle f_{900}/f_{1500}\rangle_{out}$ remains a useful empirical measurement for estimating the ionizing photon budget with knowledge of the UV luminosity function. In order to estimate the quantity more closely tied to reionization models, f_{esc}, we model the underlying

[1]The 13 LyC individual detections had the highest f_{900} out of the parent sample of 120.

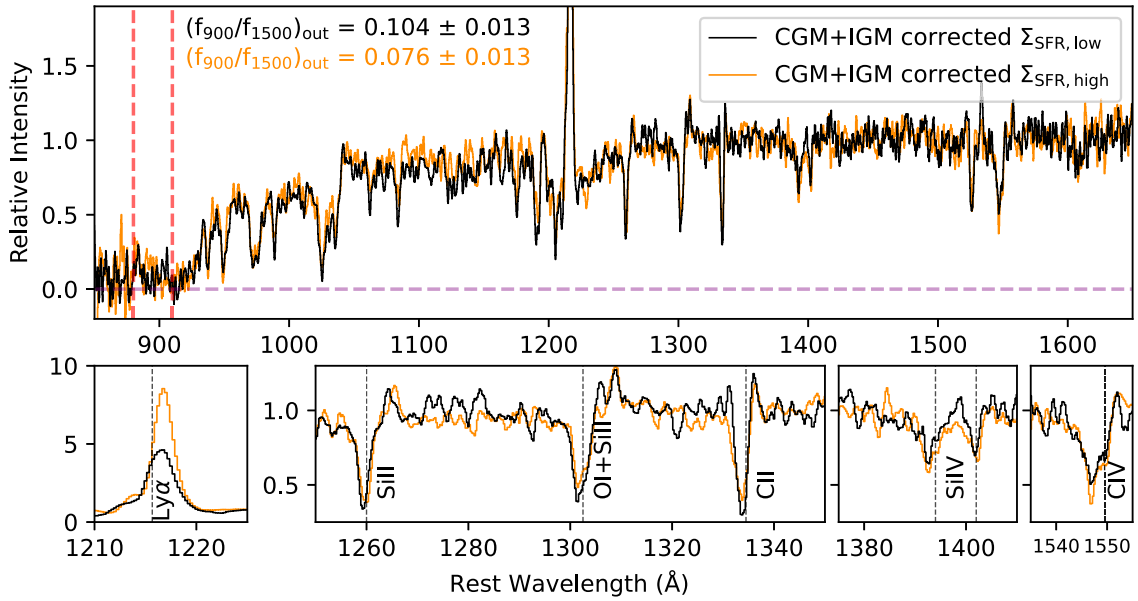

Figure 3. Composite spectra of the two KLCS *HST* subsamples binned in Σ_{SFR}. The $\Sigma_{SFR,\,low}$ composite, containing objects with the lowest Σ_{SFR}, is displayed in black, while $\Sigma_{SFR,\,high}$, containing objects with the highest Σ_{SFR}, is displayed in orange. The LyC spectral region, which defines the f_{900} measurement, is within the dashed, red lines. Top: the full composites, normalized to f_{1500}. Bottom: the same composites as above with wavelength and intensity limits set to highlight specific spectral features. From left to right, the panels highlight Lyα; Si IIλ1260, O Iλ1302 +Si IIλ1304, and C IIλ1334; Si IV$\lambda\lambda$1393, 1402; and C IVλ1548, 1550.

stellar populations of these galaxies as well as the structure of the neutral-phase ISM. Following Steidel et al. (2018) and Pahl et al. (2021), we use stellar-population synthesis models from BPASS (BPASS v2.1; Eldridge et al. 2017) together with the SMC attenuation relation (Gordon et al. 2003) at a range of $E(B-V)$ to estimate the intrinsic production rate of ionizing photons, together with geometric ISM modelling according to the 'holes' model (also see Reddy et al. 2016b, 2022). While the free parameters in the fit include continuum reddening in the foreground gas $E(B-V)_{cov}$, H I column density $\log(N_{HI}/cm^{-2})$, and covering fraction of neutral gas and dust f_c, in this work we are specifically interested in f_{esc}, defined as $f_{esc} = 1 - f_c$ for the 'holes' ISM model. Best-fitting values of $\langle f_{esc}\rangle = 0.120 \pm 0.009$ for $\Sigma_{SFR,\,low}$ and $\langle f_{esc}\rangle = 0.122 \pm 0.010$ for $\Sigma_{SFR,\,high}$ are shown as green points in Fig. 4, presented as a function of median Σ_{SFR} (see right-hand panel of Fig. 2). Here, the f_{esc} estimates assuming an SMC attenuation relation and third-quartile IGM + CGM transparency are adopted as fiducial. The estimates of f_{esc} and $\langle f_{900}/f_{1500}\rangle_{out}$ for our fiducial model are also provided in Table 2 for the $\Sigma_{SFR,\,low}$ and $\Sigma_{SFR,\,high}$ composites.

We do not find a significant trend of f_{esc} with Σ_{SFR} within the KLCS *HST* sample. We compare this trend to the f_{esc}–Σ_{SFR} relation from 'Model II' of Naidu et al. (2020). This model used Copernicus complexio Low Resolution dark-matter simulations (Hellwing et al. 2016; Sawala et al. 2016) together with assumptions of SFR (Tacchella et al. 2018) and a relation between galaxy size and halo size, and was constrained using a variety of observational data on reionization including the contaminated $f_{esc} = 0.09 \pm 0.01$ measurement from Steidel et al. (2018). This relation from Naidu et al. (2020) is $f_{esc} = 1.6\Sigma_{SFR}^{0.4}$. We display this relation as a black dashed line in Fig. 4. Despite the elevated f_{esc} measurements drawn from the KLCS *HST* sample compared to an unbiased KLCS, our $\Sigma_{SFR,\,high}$ measurement of f_{esc} falls significantly below the value predicted by the Naidu et al. (2020) relation for the same Σ_{SFR}. This 10σ deviation may be caused by low-redshift interlopers contributing to an elevated f_{esc} from Steidel et al. (2018), which Naidu et al. (2020) used as a constraint for the model fit, however, the difference between the Steidel et al. (2018) f_{esc} and the uncontaminated measurement from Pahl et al. (2021) is only 30 per cent.

We additionally measure f_{esc} using an alternative attenuation relation and average (as opposed to third-quartile) transparency of the IGM + CGM. These results, including attenuation relations from Reddy et al. (2016a), are displayed alongside the fiducial model in Fig. 4. This second set of assumptions also does not result in a significant trend in f_{esc} across the two Σ_{SFR} bins.

While the measurements of the ionizing spectral region do not indicate a dependence of ionizing photon escape on Σ_{SFR}, the longer rest-UV wavelength spectral features in the lower panels of Fig. 3 appear qualitatively distinct for the two bins in Σ_{SFR}. We measure the equivalent widths of prominent rest-UV features such as Lyα, low-ionization interstellar absorption lines (Si IIλ1260, O Iλ1302 +Si IIλ1304, C IIλ1334, and Si IIλ1527), and high-ionization interstellar absorption lines (Si IV$\lambda\lambda$1393, 1402 and C IVλ1548, 1550) following the procedure of Pahl et al. (2020) and Kornei et al. (2010). These methods bootstrap each subsample 500 times with replacement, then perturb each individual spectrum at each pixel by a Gaussian with standard deviation set by the error spectrum. Thus, the error bars on the equivalent width measurements include both sample variance and measurement errors. We measure the Lyα equivalent width, W_λ(Lyα), using the 'emission' method from Kornei et al. (2010),[2] and measure absorption line equivalent widths by integrating the absorption profile between ±5Å of the line centre after performing continuum normalization using the IRAF routine *continuum*. We present the equivalent-width measurements for both composites in Table 2. W_λ(Lyα) is elevated in the $\Sigma_{SFR,\,high}$ composite

[2]Lyα flux was integrated between the wavelength values that the Lyα profile intersected the blue-side continuum value (average flux density between 1220 Å; − 1180 Å); and the red-side continuum value (average flux density between 1225 Å; − 1255 Å).

Table 3. Properties of the KLCS *HST* sample, split into two bins of $\Sigma_{\rm SFR}$.

	$z_{\rm sys}$	$r_{\rm e}$ (kpc)	SFR ($M_\odot yr^{-1}$)	$\Sigma_{\rm SFR}$ ($M_\odot yr^{-1} kpc^{-2}$)	W_λ(Lyα) (Å)	$L_{\rm UV}/L^*_{\rm UV}$	$\langle f_{900}/f_{1500}\rangle_{\rm obs}$
				$\Sigma_{\rm SFR,\,low}$			
Q1549-C10	3.1894	1.55 ± 0.17	10.0 ± 1.5	0.66 ± 0.18	23.2	0.75	0.022 ± 0.016
Q0933-MD83	2.8800	1.64 ± 0.14	12.0 ± 4.3	0.71 ± 0.28	3.8	0.60	0.150 ± 0.041
Westphal-MMD45	2.9357	1.51 ± 0.07	13.0 ± 5.1	0.90 ± 0.37	− 19.1	1.42	0.086 ± 0.023
Q1549-C27	2.9256	1.30 ± 0.05	10.0 ± 1.9	0.94 ± 0.19	14.5	0.88	− 0.014 ± 0.019
Westphal-CC38	3.0729	1.71 ± 0.11	19.0 ± 4.1	1.03 ± 0.26	8.6	1.00	0.056 ± 0.013
DSF2237b-MD60	3.1413	1.75 ± 0.14	20.0 ± 5.3	1.04 ± 0.32	7.2	0.67	0.090 ± 0.018
Westphal-CC41	3.0268	1.22 ± 0.07	10.0 ± 3.7	1.07 ± 0.42	9.5	0.62	− 0.031 ± 0.022
Q0933-C22	3.1639	1.08 ± 0.13	9.0 ± 0.7	1.23 ± 0.31	57.6	0.73	− 0.008 ± 0.020
DSF2237b-M15	3.4034	0.77 ± 0.14	5.0 ± 0.9	1.35 ± 0.55	6.7	0.65	− 0.010 ± 0.031
Westphal-CC53	2.8070	1.19 ± 0.07	12.0 ± 3.9	1.36 ± 0.46	− 12.3	0.49	0.013 ± 0.029
Q1549-C8	2.9373	0.81 ± 0.05	9.0 ± 3.3	2.16 ± 0.85	− 10.4	0.54	0.017 ± 0.030
Q1422-d57	2.9461	0.92 ± 0.14	12.0 ± 2.2	2.24 ± 0.79	52.8	0.30	0.294 ± 0.103
Westphal-MM37	3.4215	1.38 ± 0.08	27.0 ± 5.6	2.25 ± 0.53	7.4	1.23	0.046 ± 0.009
Westphal-CC32	3.1924	1.27 ± 0.02	23.0 ± 6.2	2.27 ± 0.61	15.6	1.40	0.009 ± 0.009
DSF2237b-D13	2.9216	0.72 ± 0.05	8.0 ± 1.6	2.44 ± 0.58	− 3.8	0.58	0.077 ± 0.019
Q1422-d42	3.1369	1.18 ± 0.03	22.0 ± 4.9	2.51 ± 0.57	− 10.5	0.47	0.142 ± 0.038
Q0933-C18	2.9261	1.66 ± 0.12	44.0 ± 12.0	2.55 ± 0.78	− 13.0	0.76	0.015 ± 0.030
				$\Sigma_{\rm SFR,\,high}$			
Q1422-c63	3.0591	1.06 ± 0.20	20.0 ± 2.4	2.81 ± 1.11	− 0.1	0.28	− 0.005 ± 0.069
Q1422-md119	2.7506	1.45 ± 0.15	39.0 ± 4.5	2.96 ± 0.69	− 5.0	0.51	0.084 ± 0.084
DSF2237b-C29	3.0999	0.90 ± 0.06	16.0 ± 5.0	3.18 ± 1.07	27.8	0.64	− 0.036 ± 0.018
DSF2237b-MD38	3.3278	1.81 ± 0.11	74.0 ± 13.3	3.60 ± 0.78	− 13.8	1.47	0.075 ± 0.009
Q1422-d68	3.2865	0.59 ± 0.05	10.0 ± 2.0	4.57 ± 1.19	153.4	0.88	0.200 ± 0.028
Q0933-D23	3.2241	1.07 ± 0.06	33.0 ± 7.3	4.58 ± 1.13	− 14.9	1.29	0.003 ± 0.016
Q1422-d45	3.0717	0.97 ± 0.02	33.0 ± 7.9	5.55 ± 1.35	0.3	1.38	0.000
Westphal-DD28	3.0206	0.71 ± 0.03	19.0 ± 2.8	6.04 ± 1.02	− 14.6	1.62	− 0.036 ± 0.017
Q0933-D12	2.9242	0.82 ± 0.09	29.0 ± 3.3	6.90 ± 1.76	3.5	1.13	0.028 ± 0.025
Westphal-MM38	2.9247	0.48 ± 0.04	13.0 ± 5.7	8.88 ± 4.19	− 7.0	0.64	− 0.000
Q0933-D26	3.2662	0.42 ± 0.04	10.0 ± 1.2	8.88 ± 1.87	16.0	0.87	0.052 ± 0.027
Q0933-C27	3.5463	0.61 ± 0.04	21.0 ± 3.5	8.97 ± 1.94	46.6	0.59	− 0.042 ± 0.021
Q1422-c70	3.1286	0.41 ± 0.09	10.0 ± 2.8	9.28 ± 4.66	6.3	0.42	0.020 ± 0.056
Q1549-D3	2.9373	0.48 ± 0.01	14.0 ± 1.7	9.66 ± 1.31	8.7	1.16	0.056 ± 0.009
Q1549-C25	3.1526	0.39 ± 0.02	10.0 ± 1.3	10.41 ± 1.67	16.6	0.74	0.083 ± 0.019
Q0933-MD75	2.9131	0.32 ± 0.03	8.0 ± 0.9	12.40 ± 2.74	76.9	0.89	0.095 ± 0.023
Westphal-CC46	3.2608	0.67 ± 0.01	56.0 ± 10.3	19.66 ± 3.66	1.2	2.33	0.004 ± 0.006
Q1549-D7	2.9362	0.32 ± 0.01	29.0 ± 10.7	43.82 ± 16.63	11.5	1.07	0.001 ± 0.018

Individual detections are highlighted in bold.

compared to the $\Sigma_{\rm SFR,\,low}$ composite, while W_λ(LIS) decreases and W_λ(HIS) increase. However, none of the differences is significant. When the bootstrapping is removed from the error determinations to test the contribution of sample variance, the elevation in W_λ(Lyα) and W_λ(HIS) in $\Sigma_{\rm SFR,\,high}$ become significant. The lack of correlation between $f_{\rm esc}$ and $\Sigma_{\rm SFR}$, despite the trends in W_λ(Lyα), as well as the large sample variance in the equivalent width measurements, motivate a closer examination of how representative the KLCS *HST* sample is and its ability to recover a significant relation between $f_{\rm esc}$ and $\Sigma_{\rm SFR}$.

5 DISCUSSION

In this section, we judge our ability to recover trends between galaxy properties and ionizing photon escape using the KLCS *HST* sample, and perform simulations to determine the minimum sample size for performing these types of analyses.

W_λ(Lyα) is a well-established tracer of LyC escape in $z \sim 3$ galaxies. In the full KLCS sample, both $\langle f_{900}/f_{1500}\rangle_{\rm out}$ and $f_{\rm esc}$ are strongly correlated with W_λ(Lyα), measured across four equal-sized bins of W_λ(Lyα) (Steidel et al. 2018; Pahl et al. 2021). This correlation has also been found in other LyC surveys at $z \sim 3-4$ (Marchi et al. 2017, 2018; Fletcher et al. 2019), and is motivated physically by the similar modulation of escaping LyC and Lyα photons by the neutral gas covering fraction (Reddy et al. 2016b; Gazagnes et al. 2020; Steidel et al. 2018). 'Holes' in the ISM and CGM, free of H I and dust, would provide clear channels for both LyC and Lyα photons to escape in the observer's direction. None the less, Lyα photons may also escape off-resonance, explaining the scatter in the ratio of escaping Lyα to escaping LyC. For these reasons, we use the relationship between W_λ(Lyα) and $\langle f_{900}/f_{1500}\rangle_{\rm out}$ as an indicator of the robustness of the KLCS *HST* sample, such that, if we can recover the correlations between $\langle f_{900}/f_{1500}\rangle_{\rm out}$ and W_λ(Lyα), the composition and size of the sample is appropriate for measuring the correlation between $f_{\rm esc}$ and $\Sigma_{\rm SFR}$ presented in Section 4.

We split the KLCS *HST* sample into two bins of W_λ(Lyα), identical in size to those of $\Sigma_{\rm SFR,\,low}$ and $\Sigma_{\rm SFR,\,high}$. $W_\lambda(\text{Ly}\alpha)_{\rm low}$ contains the 17 objects with the lowest W_λ(Lyα) measurements ($W_\lambda(\text{Ly}\alpha)_{\rm med} = -7.0 \pm 3.8$), and $W_\lambda(\text{Ly}\alpha)_{\rm high}$ contains the 18 objects with the highest W_λ(Lyα) measurements ($W_\lambda(\text{Ly}\alpha)_{\rm med} = 15.8 \pm 6.1$). We constructed composite spectra and performed corrections for the effects of the IGM + CGM as described in Section 4. The resulting

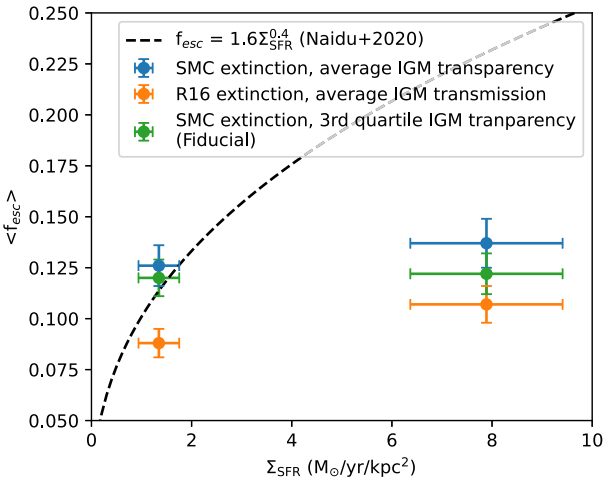

Figure 4. f_{esc} measurements for the two Σ_{SFR} composite spectra. The measurements assuming SMC extinction and third quartile IGM + CGM transparency, our fiducial model, are displayed in green. Additional measurements including a Reddy et al. (2016a) attenuation relation and average IGM + CGM transparency are shown as blue and orange trend lines. The f_{esc}–Σ_{SFR} relation from 'Model II' of Naidu et al. (2020) is shown as a dashed, black line.

$\langle f_{900}/f_{1500}\rangle_{out}$ measurements are 0.11 ± 0.02 and 0.11 ± 0.02 for $W_\lambda(\mathrm{Ly}\alpha)_{low}$ and $W_\lambda(\mathrm{Ly}\alpha)_{high}$, respectively. This lack of correlation between $\langle f_{900}/f_{1500}\rangle_{out}$ and $W_\lambda(\mathrm{Ly}\alpha)$ indicates that the KLCS *HST* sample is not capable of recovering well-established relationships between LyC escape and key galaxy properties (i.e. $W_\lambda(\mathrm{Ly}\alpha)$). We repeat this experiment with two bins of increasing L_{UV}, which is found to be strongly anticorrelated with $\langle f_{900}/f_{1500}\rangle_{out}$ in the full KLCS (Steidel et al. 2018; Pahl et al. 2021). We measured $\langle f_{900}/f_{1500}\rangle_{out} = 0.12 \pm 0.02$ from the composite made of the 17 galaxies with the lowest L_{UV}, and $\langle f_{900}/f_{1500}\rangle_{out} = 0.12 \pm 0.02$ from the composite made of the 18 galaxies with the highest L_{UV}, supporting the assertion that the KLCS *HST* sample is not suitable for performing correlation analysis with ionizing-photon escape and galaxy property. Finally, we bin the sample as a function of r_e, as a correlation between LyC leakage and rest-UV size has been found in a sample of 201 galaxies from the Vimos Ultra Deep Survey at $3.5 \leq z \leq 4.3$ (Marchi et al. 2018). We measured $\langle f_{900}/f_{1500}\rangle_{out} = 0.11 \pm 0.02$ and $\langle f_{900}/f_{1500}\rangle_{out} = 0.11 \pm 0.02$ from the lower- and higher-r_e composites, respectively, finding no significant correlation between r_e and $\langle f_{900}/f_{1500}\rangle_{out}$ in the KLCS *HST* sample.

The *HST* program that defines the KLCS *HST* sample was designed to cover all 15 galaxies that were candidates for individual LyC detections in KLCS (Steidel et al. 2018). These *HST* observations yielded 22 additional KLCS galaxies with individual LyC non-detections that fell within the footprint of the *HST*/ACS and WFC3 pointings (see Section 2). Given that these LyC non-detections are included in KLCS *HST* only on the basis of their proximity to individual apparent LyC detections, they should be representative of the population of 106 galaxies with LyC non-detections in the full sample. Briefly, we consider the sample properties of the 22 individual non-detections in KLCS *HST* compared to the 84 not covered by *HST* imaging. The median $W_\lambda(\mathrm{Ly}\alpha)$ of the KLCS *HST* non-detections is 4.9 ± 2.8Å, while the median $W_\lambda(\mathrm{Ly}\alpha)$ of the non-*HST* non-detections is 3.7 ± 2.9 Å. The *HST* subsample does not appear different from the parent sample in $W_\lambda(\mathrm{Ly}\alpha)$, neither in sample median nor sample distribution. The median L_{UV}/L^*_{UV} of the *HST* and non-*HST* non-detections are 0.7 ± 0.1 and 1.04 ± 0.04, respectively. The galaxies with individual LyC non-detections observed by *HST* appear significantly fainter than the parent sample, which could affect the dynamic range of galaxy properties that the sample is probing. At the same time, the lower L_{UV} of the *HST* non detections means the constraints on $\langle f_{900}/f_{1500}\rangle_{out}$ (due to the lower average f_{1500}) are weaker for the *HST* sample. Additionally, the LyC individual detections have a median $L_{UV}/L^*_{UV} = 0.88 \pm 0.14$, fainter than that of the objects not covered by *HST* imaging. This difference in the individual LyC detections is expected considering the inverse correlation with $\langle f_{900}/f_{1500}\rangle_{out}$ and L_{UV} found in the full sample, but further contributes to KLCS *HST* representing a biased sampling of KLCS in L_{UV}. Upon stacking the *HST* non-detections, we find the resulting $\langle f_{900}/f_{1500}\rangle_{out}$ is comparable to that of the non-*HST* non-detections, despite the inverse correlation between $\langle f_{900}/f_{1500}\rangle_{out}$ and L_{UV}. In addition to being systematically fainter, the KLCS *HST* sample does not appear to follow the canonical relationship between $\langle f_{900}/f_{1500}\rangle_{out}$ and L_{UV}.

Despite the failure of KLCS *HST* to recover established trends with $\langle f_{900}/f_{1500}\rangle_{out}$ and galaxy properties due to its sample construction, we can still use the full KLCS sample to understand how to design future observing programs of sufficient size to recover robust trends. To inform future observing programs that select a subset of the KLCS sample to analyse, we created simulations that explore the feasibility of recovering trends between $\langle f_{900}/f_{1500}\rangle_{out}$ and $W_\lambda(\mathrm{Ly}\alpha)$ with a range of sample sizes. Here, we assume that a trend between $\langle f_{900}/f_{1500}\rangle_{out}$ and $W_\lambda(\mathrm{Ly}\alpha)$ must be recovered in order to confidently constrain trends between $\langle f_{900}/f_{1500}\rangle_{out}$ other galaxy properties, considering the robustness of the $\langle f_{900}/f_{1500}\rangle_{out}$-$W_\lambda(\mathrm{Ly}\alpha)$ connection in large-scale LyC studies (Steidel et al. 2018; Gazagnes et al. 2020). If a $\langle f_{900}/f_{1500}\rangle_{out}$ and $W_\lambda(\mathrm{Ly}\alpha)$ trend is not recovered, the sample is unlikely to be able to make confident claims about how $\langle f_{900}/f_{1500}\rangle_{out}$ depends on other variables.

In the following set of simulations, we assumed that the 13 objects individually detected in LyC are always included in the analysis, similar to the design of the *HST* program described in Pahl et al. (2021). We began by randomly selecting a number of objects n with individual LyC non-detections from KLCS. We added all 13 confirmed LyC individual detections to the sample, then split the sample into two equal bins of increasing $W_\lambda(\mathrm{Ly}\alpha)$, with a bin size of $(13 + n)/2$.[3] After constructing composite spectra, we performed IGM + CGM corrections using average IGM transparency for simplicity, then measured $\langle f_{900}/f_{1500}\rangle_{out}$ from the IGM + CGM corrected composites. We repeated this experiment 1000 times for different random draws of n galaxies with individual LyC non-detections in KLCS, always including the 13 confirmed LyC individual detections. For each iteration, we determined whether the subsequent $\langle f_{900}/f_{1500}\rangle_{out}$ measurements recovered a significant increase in $\langle f_{900}/f_{1500}\rangle_{out}$ across the two bins of increasing $W_\lambda(\mathrm{Ly}\alpha)$ as reported in Steidel et al. (2018) and Pahl et al. (2021). A 1σ increase was defined as

$$(\langle f_{900}/f_{1500}\rangle_{out,1} - \langle f_{900}/f_{1500}\rangle_{out,2}) > \sqrt{(\sigma_{fout,1})^2 + (\sigma_{fout,2})^2}, \quad (2)$$

where the subscript '1' denotes measurements associated with the $W_\lambda(\mathrm{Ly}\alpha)_{high}$ bin and the subscript '2' denotes measurements of the $W_\lambda(\mathrm{Ly}\alpha)_{low}$ bin, and σ_{fout} is the error on the corresponding $\langle f_{900}/f_{1500}\rangle_{out}$ measurement. If this condition was met, we counted

[3]In the cases where the total sample size was odd, the higher $W_\lambda(\mathrm{Ly}\alpha)$ bin had one more object than the lower $W_\lambda(\mathrm{Ly}\alpha)$ bin.

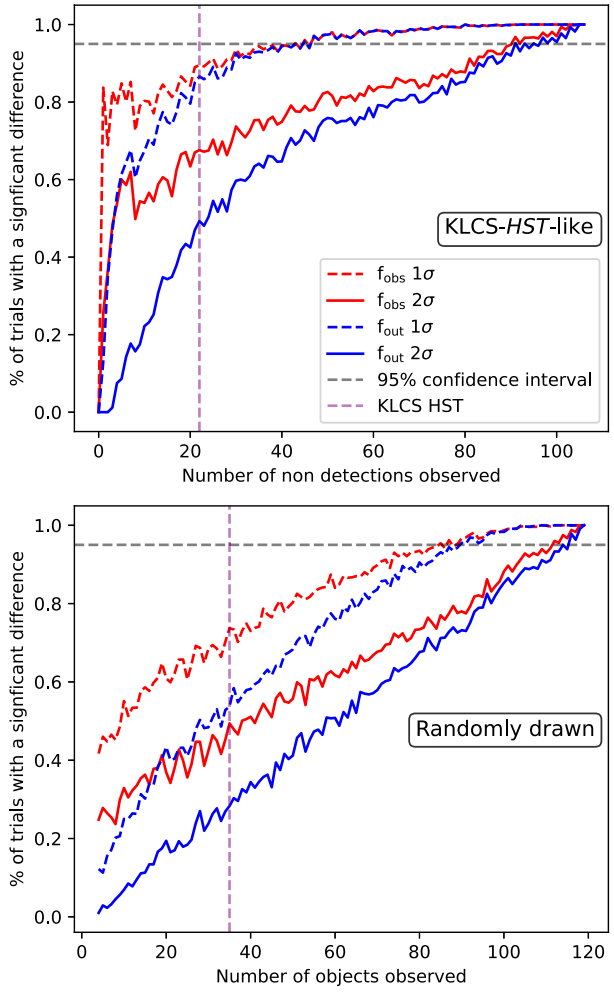

Figure 5. Simulations to determine if a subsample of a given size is sufficient to recover an increase of $\langle f_{900}/f_{1500}\rangle$ across two equal bins of W_λ(Lyα). A successful trial was defined as a case in which the $\langle f_{900}/f_{1500}\rangle$ measurement of the upper W_λ(Lyα) composite was greater than the corresponding measurement from the lower W_λ(Lyα) composite at a 1σ confidence level for the dashed lines, and 2σ for the solid lines. The blue curves represent the likelihood of significant correlations recovered for $\langle f_{900}/f_{1500}\rangle_{out}$, which includes corrections for attenuation from the IGM + CGM attenuation, while the red curves use simply $\langle f_{900}/f_{1500}\rangle_{obs}$. For each sample size, 1000 random draws were performed to determine the per cent chance of success. Top: KLCS-*HST*-like sample construction, which includes 13 individually detected LyC objects for every trial and a number of n non-detections, for a total sample size of 13 + n. The number of non-detections included in KLCS *HST* is 22, represented by a purple, vertical, dashed line. Bottom: sample construction includes n randomly drawn galaxies from KLCS. Here, KLCS *HST* is represented by a purple, vertical, dashed line at 35, ignoring the oversampling of individually detected objects in KLCS *HST*.

the trial as a 'success.' The proportion of trials that successfully recovered a 1σ increase in $\langle f_{900}/f_{1500}\rangle_{out}$ for a range of n is presented as the blue, dashed curve in the upper panel of Fig. 5. For $n = 22$, identical to the number of non-detections included in KLCS *HST* (and plotted as a vertical, purple, dashed line), a 1σ increase in $\langle f_{900}/f_{1500}\rangle_{out}$ across two bins of increasing W_λ(Lyα) was found in 86.6 per cent of random draws. In order to ensure that a 1σ increase is recovered >95 per cent of the time, $n = 45$ was required, for a total sample size of 58. For each iteration, we also measured the ratio of ionizing to non-ionizing flux density before IGM + CGM corrections, or $\langle f_{900}/f_{1500}\rangle_{obs}$, to explore the effects of the uncertainty of the IGM and CGM corrections on the simulations. The percentage of trials that successfully measured an increase in $\langle f_{900}/f_{1500}\rangle_{obs}$ is presented as a function of n in the red, dashed line in Fig. 5. As expected, because of the reduced uncertainty, removing corrections for the attenuation of the IGM + CGM induced 'significant' differences in $\langle f_{900}/f_{1500}\rangle_{obs}$ across the two W_λ(Lyα) bins more often. We additionally include solid curves in Fig. 5 that represent identical simulations with a stricter success threshold of 2σ (i.e. a difference in $\langle f_{900}/f_{1500}\rangle_{out}$ for the two bins that exceeds twice the error on the difference). For $n = 22$, a 2σ increase in $\langle f_{900}/f_{1500}\rangle_{out}$ was recovered for 49.3 per cent of the iterations, while $n = 91$ (total sample size of 104) was required for a 2σ increase to be recovered for >95 per cent of iterations.

We performed a similar set of simulations without the stipulation that objects with individual LyC detections in the KLCS are preferentially observed. In this case, the subsamples for analysis were drawn randomly from the 120 galaxies in the full KLCS sample. This set of simulations is comparable to a survey that is blind to the ionizing properties of the galaxies before analysis and stacking. Here, we chose n galaxies from KLCS such that n is the complete sample size of the subsample. The other steps of this set of simulations were identical to those described above, including the binning as a function of W_λ(Lyα), generation of composite spectra, correcting for the IGM + CGM, and measuring $\langle f_{900}/f_{1500}\rangle_{out}$. The percentage of trials that recovered a 1σ increase in $\langle f_{900}/f_{1500}\rangle_{out}$ across the two bins of increasing W_λ(Lyα) is presented as a function of n using a dashed, blue curve in the bottom panel of Fig. 5. Here, $n = 35$ would be comparable to an KLCS *HST*-like program of 13 LyC detections and 22 LyC non-detections, but in this case the individual LyC detections are not oversampled. For $n = 35$, a 1σ increase in $\langle f_{900}/f_{1500}\rangle_{out}$ across the two bins of increasing W_λ(Lyα) was only seen in 53.7 per cent of the iterations. The difference between this set of simulations and the preceding one indicates that preferentially observing LyC detections increases the ability to measure trends with $\langle f_{900}/f_{1500}\rangle_{out}$ and galaxy property at fixed sample size. To recover a 1σ difference in 95 per cent of trials, $n = 90$ objects were required. Similar to the upper panel, we also include curves that test correlation of $\langle f_{900}/f_{1500}\rangle_{obs}$ with W_λ(Lyα) and a stricter 2σ calculation of trial success.

In summary, despite the tendency for KLCS *HST*-like samples to recover expected trends between $\langle f_{900}/f_{1500}\rangle_{out}$ and W_λ(Lyα), we do not find a significant correlation between $\langle f_{900}/f_{1500}\rangle_{out}$ and W_λ(Lyα) in KLCS *HST*. This result is somewhat unexpected, considering this lack of correlation is only recovered in ∼ 13 per cent of trials at similar sample size. The fact that we cannot recover the connection between $\langle f_{900}/f_{1500}\rangle_{out}$ and W_λ(Lyα) in the KLCS *HST* sample calls into question the robustness of the lack of correlation found between f_{esc} and Σ_{SFR} in Section 4. Our simulations show that we require a larger sample size to ensure that a significant correlation is recovered between $\langle f_{900}/f_{1500}\rangle_{out}$ and W_λ(Lyα), which we have assumed is a requirement to discern a significant trend between f_{esc} and Σ_{SFR}. Accordingly, a larger sample size is required to make robust statements about the connection between f_{esc} and Σ_{SFR}. The simulations presented in this section can be used to dictate future *HST* LyC observing programs. However, these results assume a parent sample with spectra of similar quality to KLCS, and having the same intrinsic correlation. With better quality spectra or a sample that covers a larger dynamic range of galaxy property (e.g. Σ_{SFR}, L_{UV}), the necessary sample size may decrease. None the less, these results provide insight into how measurement uncertainty, IGM sightline variability, and sample size can affect eventual measurements of the connection between f_{esc} and galaxy properties.

6 SUMMARY

The timeline of reionization remains uncertain, as the main sources that drive the process are still debated. Estimating f_{esc} in samples of lower-redshift analogues and studying how their properties connect with f_{esc} is a fruitful endeavour to distinguish among various models of reionization. In order to explore the potential connection between f_{esc} and Σ_{SFR}, which is well motivated by the physics of star formation feedback (e.g. Ma et al. 2016; Sharma et al. 2016; Kakiichi & Gronke 2021), we examined a sample of 35 galaxies drawn from the KLCS survey that have been shown to be free of line-of-sight contamination based on *HST* imaging. We measured r_e using Sérsic profile fits to high-resolution, V_{606} images, and SFR from SED fits to ground- and space-based photometry. We split the sample into two bins of Σ_{SFR}, and constructed composite rest-UV spectra to examine whether their ionizing and non-ionizing rest-UV spectral features depend on the sample median Σ_{SFR}. The main results of this work are as follows:

(i) We measure no significant difference in f_{esc} for spectral composites constructed from the KLCS *HST* sample split into two bins of Σ_{SFR}. This null result is confirmed for a range of assumptions regarding IGM transparency and dust attenuation. Redward of LyC, we measure an elevated W_λ(Lyα) and W_λ(HIS) in the composite characterized by the larger Σ_{SFR}, although these differences between the two Σ_{SFR} subsamples were not significant after considering sample variance.

(ii) We measure no significant difference in f_{esc} across two composites binned as a function of W_λ(Lyα), despite f_{esc}-W_λ(Lyα) relationships found in the full KLCS, and other LyC surveys (e.g. Fletcher et al. 2019; Gazagnes et al. 2020). Repeating the experiment using two bins of L_{UV}, we also find no significant difference in f_{esc} between composite spectra. These results indicate that the KLCS *HST* sample is unable to robustly constrain correlations between f_{esc} and other galaxy properties, including Σ_{SFR}.

(iii) We find that a sample of >58 galaxies (13 galaxies individually detected in LyC, 45 individually undetected) would be required to recover a significant positive change in $\langle f_{900}/f_{1500}\rangle_{out}$ among in two subsamples binned by W_λ(Lyα) > 95 per cent of the time. This recommendation is based on stacking simulations using the full KLCS, randomly drawing 45 individual LyC non-detections while always including the 13 LyC detections, similar to the construction of the KLCS *HST* sample. With a KLCS-*HST*-like sample of 13 LyC detections and 22 randomly drawn non-detections, a significant correlation is recovered in only 86.6 per cent of realizations. Here, the actual KLCS *HST* sample corresponds to one of the $\sim$ 13 per cent of trials in which a correlation would not be recovered.

(iv) We repeat the stacking simulations without the assumption that the 13 individual LyC detections are preferentially observed, and find that a sample of >90 objects is required to recover a 1σ increase in $\langle f_{900}/f_{1500}\rangle_{out}$ across two bins of increasing W_λ(Lyα) in >95 per cent of trials. These simulations are performed by drawing 90 objects randomly from KLCS before binning and stacking, and did not include all detections in every mock sample. These simulations can be used to inform future LyC surveys aimed at studying dependencies of f_{esc} on other galaxy properties, although the recommended numbers depend on spectral SNR and dynamic range of the sample.

We have demonstrated that the KLCS *HST* sample is unfortunately not appropriate for recovering possible trends between f_{esc} and Σ_{SFR}, due to a combination of small sample size and non-representativeness in terms of the distribution of quantities such as L_{UV} at fixed W_λ(Lyα). We have also outlined what must be done to further explore the f_{esc}-Σ_{SFR} connection: more objects are needed with *HST*-resolution imaging appropriate for accurate size estimates and contamination rejection, combined with deep, rest-UV spectra to estimate f_{esc} in stacked composites with sufficient objects in each bin. We will better constrain these important trends using KLCS after more individual LyC non-detections are followed up by *HST*.

We acknowledge support from NSF AAG grants 0606912, 0908805, 1313472 2009313, 2009085, and 2009278. Support for program *HST*-GO-15287.001 was provided by NASA through a grant from the Space Telescope Science Institute, which is operated by the Associations of Universities for Research in Astronomy, Incorporated, under NASA contract NAS5-26555. CS was supported in part by the Caltech/JPL President's and Director's program. Based on observations obtained with MegaPrime/MegaCam, a joint project of CFHT and CEA/IRFU, at the Canada-France-Hawaii Telescope (CFHT) which is operated by the National Research Council (NRC) of Canada, the Institut National des Science de l'Univers of the Centre National de la Recherche Scientifique (CNRS) of France, and the University of Hawaii. This work is based in part on data products produced at Terapix available at the Canadian Astronomy Data Centre as part of the CFHT Legacy Survey, a collaborative project of NRC and CNRS. We wish to extend special thanks to those of Hawaiian ancestry on whose sacred mountain we are privileged to be guests. Without their generous hospitality, most of the observations presented herein would not have been possible.

DATA AVAILABILITY STATEMENT

The *HST* data presented in this article are publicly available from the Mikulski Archive for Space Telescopes. The ground-based data presented here will be shared on reasonable request to the corresponding author.

REFERENCES

Adelberger K. L., Steidel C. C., Shapley A. E., Hunt M. P., Erb D. K., Reddy N. A., Pettini M., 2004, ApJ, 607, 226
Bertin E., Arnouts S., 1996, A&AS, 117, 393
Bian F., Fan X., McGreer I., Cai Z., Jiang L., 2017, ApJ Letters, 837, L12
Bielby R. et al., 2012, A&A, 545, A23
Borthakur S., Heckman T. M., Leitherer C., Overzier R. A., 2014, Science, 346, 216
Bradley L. et al., 2020, astropy/photutils: 1.0.1, Zenodo
Bruzual G., Charlot S., 2003, MNRAS, 344, 1000
Calzetti D., Armus L., Bohlin R. C., Kinney A. L., Koornneef J., Storchi-Bergmann T., 2000, ApJ, 533, 682
De Barros S. et al., 2016, A&A, 585, 51
Du X. et al., 2018, ApJ, 860, 75
Eldridge J. J., Stanway E. R., Xiao L., McClelland L. A., Taylor G., Ng M., Greis S. M., Bray J. C., 2017, Publ. Astron. Soc. Aust., 34, 61
Fan X., Carilli C. L., Keating B., 2006, ARA&A, 44, 415
Finkelstein S. L. et al., 2019, ApJ, 879, 36
Fletcher T. J., Tang M., Robertson B. E., Nakajima K., Ellis R. S., Stark D. P., Inoue A., 2019, ApJ, 878, 87
Gazagnes S., Chisholm J., Schaerer D., Verhamme A., Izotov Y., 2020, A&A, 639, A85
Gillman S. et al., 2020, MNRAS, 492, 1492
Gordon K. D., Clayton G. C., Misselt K. A., Landolt A. U., Wolff M. J., 2003, ApJ, 594, 279
Grazian A. et al., 2017, A&A, 602, A18
Hellwing W. A., Frenk C. S., Cautun M., Bose S., Helly J., Jenkins A., Sawala T., Cytowski M., 2016, MNRAS, 457, 3492
Izotov Y. I., Schaerer D., Thuan T. X., Worseck G., Guseva N. G., Orlitova I., Verhamme A., 2016, MNRAS, 461, 3683

Izotov Y. I., Worseck G., Schaerer D., Guseva N. G., Thuan T. X., Fricke K. J., Verhamme A., Orlitová I., 2018, MNRAS, 478, 4851
Izotov Y. I., Worseck G., Schaerer D., Guseva N. G., Chisholm J., Thuan T. X., Fricke K. J., Verhamme A., 2021, MNRAS, 503, 1734
Kakiichi K., Gronke M., 2021, ApJ, 908, 30
Kornei K. A., Shapley A. E., Erb D. K., Steidel C. C., Reddy N. A., Pettini M., Bogosavljević M., 2010, ApJ, 711, 693
Law D. R., Steidel C. C., Shapley A. E., Nagy S. R., Reddy N. A., Erb D. K., 2012, ApJ, 745, 85
Ma X., Hopkins P. F., Kasen D., Quataert E., Faucher-Giguère C. A., Kereš D., Murray N., Strom A., 2016, MNRAS, 459, 3614
Marchi F. et al., 2017, A&A, 601, 73
Marchi F. et al., 2018, A&A, 614, 11
Mostardi R. E., Shapley A. E., Steidel C. C., Trainor R. F., Reddy N. A., Siana B., 2015, ApJ, 810, 107
Naidu R. P., Tacchella S., Mason C. A., Bose S., Oesch P. A., Conroy C., 2020, ApJ, 892, 109
Nakajima K., Ellis R. S., Robertson B. E., Tang M., Stark D. P., 2020, ApJ, 889, 12
Oke J. B., Gunn J. E., 1983, ApJ, 266, 713
Oke J. B. et al., 1995, Publ. Astron. Soc. Pac., 107, 375
Onodera M. et al., 2016, ApJ, 822, 42
Pahl A. J., Shapley A., Faisst A. L., Capak P. L., Du X., Reddy N. A., Laursen P., Topping M. W., 2020, MNRAS, 493, 3194
Pahl A. J., Shapley A., Steidel C. C., Chen Y., Reddy N. A., 2021, MNRAS, 505, 2447
Parsa S., Dunlop J. S., McLure R. J., 2018, MNRAS, 474, 2904
Peng C. Y., Ho L. C., Impey C. D., Rix H.-W., 2002, AJ, 124, 266
Peng C. Y., Ho L. C., Impey C. D., Rix H. W., 2010, AJ, 139, 2097
Reddy N. A., Pettini M., Steidel C. C., Shapley A. E., Erb D. K., Law D. R., 2012, ApJ, 754, 25
Reddy N. A., Steidel C. C., Pettini M., Bogosavljević M., 2016a, ApJ, 828, 107
Reddy N. A., Steidel C. C., Pettini M., Bogosavljević M., Shapley A. E., 2016b, ApJ, 828, 108
Reddy N. A. et al., 2018, ApJ, 869, 92
Reddy N. A. et al., 2022, ApJ, 296, 36
Robertson B. E., Ellis R. S., Furlanetto S. R., Dunlop J. S., 2015, ApJ , 802, L19
Salpeter E. E., 1955, ApJ, 121, 161
Sanders R. L. et al., 2015, ApJ, 799, 138
Sawala T. et al., 2016, MNRAS, 457, 1931
Saxena A. et al., 2021, MNRAS, 511, 120
Shapley A. E., Steidel C. C., Strom A. L., Bogosavljević M., Reddy N. A., Siana B., Mostardi R. E., Rudie G. C., 2016, ApJ, 826, L24
Sharma M., Theuns T., Frenk C., Bower R., Crain R., Schaller M., Schaye J., 2016, MNRAS, 458, L94
Shibuya T., Ouchi M., Harikane Y., 2015, ApJS, 219, 15
Steidel C. C., Adelberger K. L., Shapley A. E., Pettini M., Dickinson M., Giavalisco M., 2003, ApJ, 592, 728
Steidel C. C., Shapley A. E., Pettini M., Adelberger K. L., Erb D. K., Reddy N. A., Hunt M. P., 2004, ApJ, 604, 534
Steidel C. C. et al., 2014, ApJ, 795, 165
Steidel C. C., Bogosavljević M., Shapley A. E., Reddy N. A., Rudie G. C., Pettini M., Trainor R. F., Strom A. L., 2018, ApJ, 869, 123
Tacchella S., Bose S., Conroy C., Eisenstein D. J., Johnson B. D., 2018, ApJ, 868, 92
Van Der Wel A. et al., 2012, ApJS, 203, 24
Vanzella E. et al., 2012, ApJ, 751, 70
Vanzella E. et al., 2016, ApJ, 821, L27
Vanzella E. et al., 2018, MNRAS, 476, L15

This paper has been typeset from a TEX/LATEX file prepared by the author.